Ultrahigh-charge electron beams from laser-irradiated solid surface

Yong Ma[a,b], Jiarui Zhao[a], Yifei Li[a], Dazhang Li[c], Liming Chen[a,d,e,f,1], Jianxun Liu[g], Stephen J. D. Dann[b], Yanyun Ma[g,1], Xiaohu Yang[g], Zheyi Ge[g], Zhengming Sheng[d,e,h], and Jie Zhang[d,e,f,1]

[a]Institute of Physics, Chinese Academy of Sciences, Beijing 100190, China; [b]Department of Physics, Lancaster University, Bailrigg LA1 4YW, United Kingdom; [c]Institute of High Energy Physics, Chinese Academy of Sciences, Beijing 100049, China; [d]Collaborative Innovation Center of Inertial Fusion Sciences and Applications, Shanghai Jiao Tong University, Shanghai 200240, China; [e]School of Physics and Astronomy, Shanghai Jiao Tong University, Shanghai 200240, China; [f]School of Physical Sciences, University of Chinese Academy of Sciences, Beijing 100049, China; [g]College of Science, National University of Defense Technology, Changsha 410073, China; and [h]Department of Physics, Scottish Universities Physics Alliance, University of Strathclyde, Glasgow G4 0NG, United Kingdom

Contributed by Jie Zhang, May 21, 2018 (sent for review January 29, 2018; reviewed by Sergei Bulanov and Yoshiaki Kato)

Compact acceleration of a tightly collimated relativistic electron beam with high charge from a laser–plasma interaction has many unique applications. However, currently the well-known schemes, including laser wakefield acceleration from gases and vacuum laser acceleration from solids, often produce electron beams either with low charge or with large divergence angles. In this work, we report the generation of highly collimated electron beams with a divergence angle of a few degrees, nonthermal spectra peaked at the megaelectronvolt level, and extremely high charge ($\sim$100 nC) via a powerful subpicosecond laser pulse interacting with a solid target in grazing incidence. Particle-in-cell simulations illustrate a direct laser acceleration scenario, in which the self-filamentation is triggered in a large-scale near–critical-density plasma and electron bunches are accelerated periodically and collimated by the ultraintense electromagnetic field. The energy density of such electron beams in high-Z materials reaches to $\sim$10^{12} J/m^3, making it a promising tool to drive warm or even hot dense matter states.

laser–plasma interaction | direct laser acceleration | ultrahigh-charge beam | high energy density | near–critical-density plasma

In studies of laser–plasma acceleration (LPA), several laser wakefield accelerator (LWFA) (1) concepts have been proposed in the last few decades, including the plasma beat wave accelerator (1, 2), the self-modulated laser wakefield accelerator (SM-LWFA) (3), the cross-modulated laser wakefield accelerator (XM-LWFA) (4), and LWFA in the bubble regime (5, 6). The successful generation of high-quality electron beams at the gigaelectronvolt scale with quasi-monoenergetic spectra has stimulated the study of LPAs worldwide (7–14). However, almost all LPA experiments and theoretical models are based on interactions between lasers and gases, limiting the beam charge to typically a few tens of picocoulombs. While the charge of the electron bunch could reach a few nanocoulombs in laser–solid interactions due to higher absorption efficiency and attempts have been made to optimize beam collimation (15–23), the beam quality still needs to be greatly improved due to large divergence angles and quasi-thermal broad energy spectra. Such electrons are usually generated via several heating mechanisms such as resonant absorption (24, 25), vacuum heating (25–27), $J\times B$ heating (28), and stochastic heating (29). Directional electron beams with nanocoulomb charge have been produced via vacuum laser acceleration (VLA) with a plasma mirror injector (30). Unfortunately, the beam collimation also suffers from the ponderomotive force of the laser pulse in vacuum during acceleration, which results in a large divergence angle (hundreds of milliradians) and a halo in the electron beam profile. Recently, a few megaelectronvolts of quasi-monoenergetic electron acceleration have been observed in femtosecond laser–solid interaction with beam divergence angles of $1^\circ-2^\circ$ (31). However, the beam charge is still limited to hundreds of picocoulombs, and the underlying physics of such acceleration remain unclear.

In this work, electron beams with extremely high beam charge of approximately 100 nC are generated in 200-TW, subpicosecond laser–solid interactions with deliberately induced preplasma. The electron beams are highly collimated with an average divergence angle $<3^\circ$ and the energy spectra are nonthermal with peaks at several megaelectronvolts. Particle-in-cell (PIC) simulations illustrate a scenario of electron acceleration in which the acceleration and confinement regimes are combined in a unique way. It is shown that electron beams are mainly produced via direct laser acceleration (DLA) (32–38) in plasma channels (39, 40) driven by the long laser pulse in a large-scale near-critical preplasma. The strong electromagnetic field inside the plasma channel confines the electron beams tightly. The significant improvement of the beam charge benefits from the persistent DLA process.

Experimental Results

The experiment was performed on Titan at the Jupiter Laser Facility at Lawrence Livermore National Laboratory (LLNL). The setup of the experiment is shown in Fig. 1. Copper block targets were irradiated by a 200-TW, subpicosecond laser at an incident angle of 72° in P polarization. The laser pedestal 3 ns

Significance

In the last three decades, the laser–plasma accelerator (LPA) has shown a rapid development owing to its super–high-accelerate gradients, which makes it a very promising compact accelerator and light source. Acceleration of a high-quality electron beam with divergence angle as small as possible and beam charge as high as possible has been a long-term goal ever since the inception of the LPA concept. However, until now the most popular acceleration scenario has failed to achieve both goals. We solved this problem and obtained tightly collimated electron beams with small divergence angle and extremely high beam charge ($\sim$100 nC) via the powerful *ps* laser pulse interacting with a solid target.

Author contributions: L.C. and J. Zhang designed research; Yong Ma, J. Zhao, Y.L., D.L., and L.C. performed research; Yong Ma, J.L., S.J.D.D., Yanyun Ma, X.Y., and Z.G. contributed new reagents/analytic tools; Yong Ma, J. Zhao, Y.L., and L.C. analyzed data; Yong Ma, L.C., and Z.S. wrote the paper; and J. Zhang facilitated the experiment and led the whole project.

Reviewers: S.B., Extreme Light Infrastructure-Beamlines; and Y.K., The Graduate School for the Creation of New Photonics Industries.

The authors declare no conflict of interest.

[1] To whom correspondence may be addressed. Email: jzhang1@sjtu.edu.cn, lmchen@iphy.ac.cn, or yanyunma@126.com.

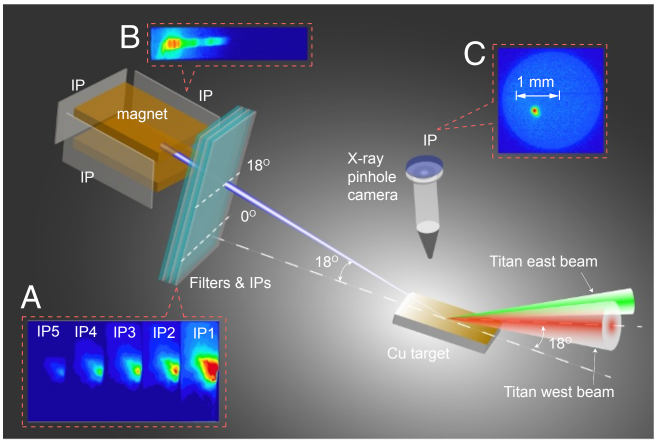

Fig. 1. Experimental setup. *Insets* show (*A*) the angular distribution of the electron beam on image plates, (*B*) the energy distribution after being deflected by the spectrometer, and (*C*) the image of the X-ray source detected by an X-ray pinhole camera.

before the main pulse was measured to be 5 ± 2 mJ at 1ω with full laser energy of 150 J and ~ 0.2 μJ at 2ω with full laser energy of 30 ± 5 J.

Highly collimated electron bunches with good pointing stability and extremely high beam charge were generated, as shown in Fig. 2*A*, using the full energy laser pulse with approximately 5 mJ prepulse. These beams were emitted along the laser specular reflection direction with an average divergence angle of 2.7° (47 mrad) FWHM. This is much smaller than those generated via the VLA mechanism in laser–solid interactions and approaching that of laser-driven wakefield acceleration from gas, which is typically $\sim$10 mrad. The beam charge can be as high as 94 nC with energy above 1.0 MeV (Figs. 2 *A*, *III* and 3*A*). This observation reveals electron bunches with a high charge and a small divergence angle. The beam current reaches $I \simeq 134$ kA by assuming the pulse length of the electron beam is the same as that of the laser pulse. This is a large fraction of the Alfv́en current limit (41, 42), which in this case is $I_A = 1.65 \times 17[\text{kA}]\sqrt{\gamma^2 - 1} = 262$ kA, where $\gamma = 9.4$ for the average energy of 5.3 MeV, as shown in Fig. 4*C*.

In addition to the generation of collimated beams (the central bright spot) in the laser specular direction, a weak plateau appears between laser specular and target normal. This indicates that the generation mechanism of the plateau electrons differs from that of the central bright spot and the energy of such electrons could be much lower. The outgoing direction of plateau electrons is energy dependent: $\sin\alpha' = (\gamma - 1/\gamma)\sin\alpha$ (43), where γ is the Lorenz factor of electrons, and α' and α are angles between the target normal and the outgoing and laser specular directions, respectively.

When increasing the prepulse energy to a few tens of millijoules, the electron beam divergence increases significantly but with a similar level of beam charge, as shown in Figs. 2*B* and 3*A*. The outgoing direction of electrons is between the laser specular and target normal. Note that the peak intensity of the 5-mJ prepulse reaches 9×10^{15} W/cm^2, which is already high enough to produce preplasma on the solid target. It seems that the preplasma scale length has an adverse effect on the beam collimation, but not on the beam charge.

To further investigate the influence of preplasma, we also gradually reduced the prepulse energy and hence the prepulse intensity. However, the 5-mJ prepulse is the smallest which can be achieved with this laser operating at 1ω. Therefore, 2ω laser pulses were used, lowering the prepulse energy to ~ 0.2 μJ with intensity below the ionization threshold. A nanosecond laser pulse was used as an additional prepulse to produce preplasma. Before the introduction of the prepulse, i.e., using the 2ω Titan west beam only, the outgoing direction of the electron beams is still along laser specular and the average divergence angle is 3.3°, which is very close to that in Fig. 2*A*. However, the beam charge decreases to an average of $\sim$1.5 nC because of much lower laser energy. Then, increasing the energy of the prepulse gradually and keeping the main pulse energy fixed at $\sim$30 J, the average FWHM divergence angle of the electron beams increases accordingly and reaches a maximum of 46.4°, while the beam charge quickly increases and then remains at the same level ($\sim$5 nC on average). This dependence of beam divergence on prepulse energy with a 30-J 2ω drive laser is similar to that with a 150-J 1ω drive laser. We conclude that even though the main pulse energy plays the key role in controlling the electron beam charge, the preplasma condition has significant effects on the beam divergence angle.

The energy spectra of the outgoing electron beams are shown in Fig. 4. In Fig. 4*A*, with the 2ω laser pulse and no preplasma, most of the electrons are low energy (<1 MeV) and the exponential decay fitting gives an effective temperature $kT = 0.5$ MeV. In the case of the 1ω laser pulse with high prepulse, the energy spectrum in Fig. 4*B* demonstrates an obvious dual-temperature distribution. Although the majority are still below 1 MeV with an effective temperature of $kT_1 = 0.7$ MeV, the high-energy tail reaches 20 MeV with a much higher effective temperature of $kT_2 = 31.9$ MeV. It is obvious that these two groups of electrons with different temperatures have been generated via different mechanisms. Low-temperature electrons might be produced by

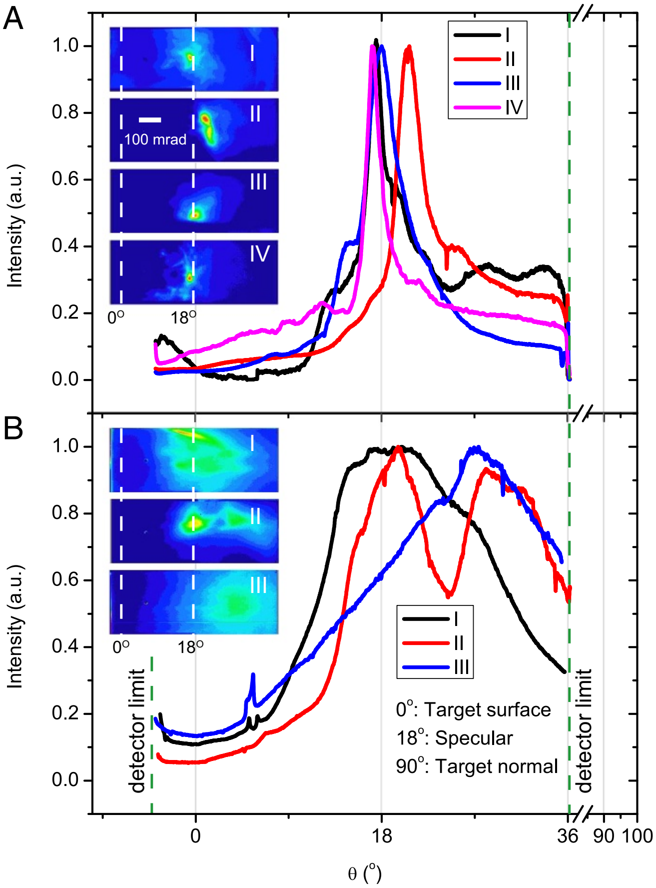

Fig. 2. Angular distribution of the electron beams with 1ω 150-J laser pulse. Prepulse energies in *A*, *I–IV* are 7 mJ, 5 mJ, 7 mJ, and 4 mJ; prepulse energies in *B*, *I–III* are 20 mJ, 32 mJ, and 82 mJ.

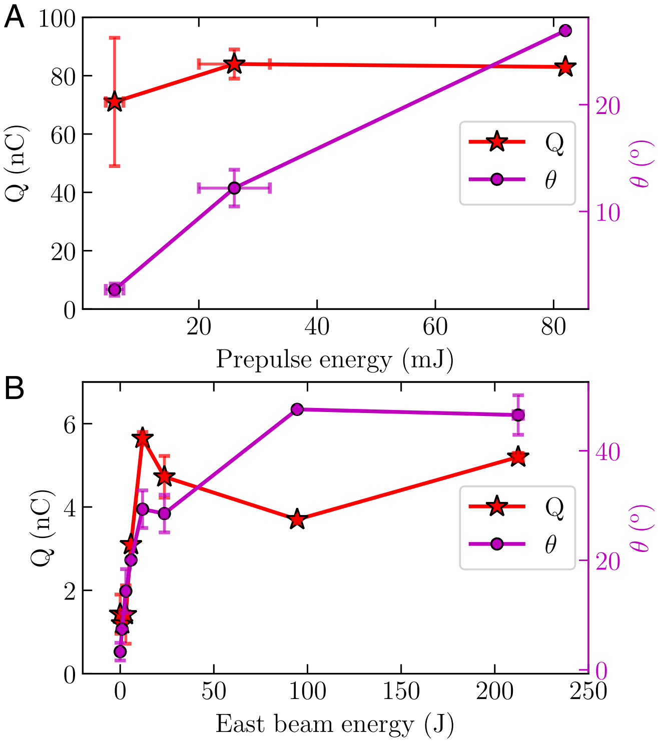

Fig. 3. Electron beam charge and divergence angle. (*A*) Dependence of electron beam charge and divergence angle on the intrinsic prepulse energy of the 1ω main pulse at 150 J. (*B*) Dependence of electron beam charge and divergence angle on prepulse (Titan east beam) energy with 2ω main pulse at 30 ± 5 J.

a laser heating process, such as resonant absorption, J×B heating, and so on. The generation of high-temperature electrons could be a result of a particular acceleration process (rather than heating). When lowering the prepulse energy of the 1ω laser pulse to 5 mJ, the spectrum becomes nonthermal with peaks at 2–6 MeV and the amount of lower-energy electrons is greatly suppressed, as shown in Fig. 4*C*. These are the same laser parameters as in Fig. 2*A* where tightly collimated electron beams with extremely high beam charge were observed.

Simulation and Discussion

To investigate the mechanism of the generation of such collimated electron beams with nonthermal spectra and extremely high beam charge, PIC simulations were performed and the results agree qualitatively with those of the experiment.

The general scenario of the interaction is shown in Fig. 5. The self-filamentation process is enhanced by grazing incidence. As the laser pulse penetrates into the near–critical-density region, the lower part of the beam, which is in the higher plasma density, is reflected by the plasma and interacts with the less affected upper part in the relatively lower density. As a consequence, the superposition of these two parts leads to a transverse self-modulation in intensity, i.e., self-filamentation, as shown in Fig. 5 *A*, *II*. As the laser pulse penetrates farther into the higher-density region, the laser pulse breaks up into three main filaments. As shown in Fig. 5 *A*, *III* at $t = 440\ T_0$, the top filament starts to be reflected and the other two keep penetrating into the overdense plasma. All three filaments drive their own plasma channels, as shown in Fig. 5 *B*, *III*. However, the two lower ones disappear eventually after the energy is fully depleted. The upper filament survives and propagates along the laser specular direction where it continuously drives its plasma channel, trapping and heating electron bunches as shown in Fig. 5 *A*, *IV* and *B*, *IV*. The electron bunching with constant spacing in the plasma channel indicates that the acceleration mechanism is similar to DLA.

To deeply understand the strong collimation of the electron beam, the transverse electromagnetic force $F_\perp \sim E_y - cB_z$ is given in Fig. 6*A*. Fig. 6*B* illustrates that the overall electromagnetic force inside the plasma channel (Fig. 6*D*) tends to focus the electron beam, which results in the self-collimation of the electron beam. Similar phenomena were also found in refs. 17 and 44.

To understand the detailed procedures of the acceleration, the electron distribution in energy gain space of (W_x, W_y) at $t = 555\ T_0$ is given in Fig. 6*E*. Here W_y and W_x are, respectively, the energy gain from the laser field which represents the DLA and the energy gain from the electrostatic field along the laser propagating direction which represents wakefield acceleration. It is very clear that the dominant acceleration mechanism is DLA since most of the electrons are located in the region where $W_y > W_x$.

The DLA mechanism was further confirmed by examining the evolution of the electron's trajectories. All of the trajectories shown in Fig. 7 are from the same randomly selected electron which performs betatron oscillation in the plasma channel. Fig. 7*B* illustrates the fact that the oscillation frequency of the longitudinal momentum is twice of that of the transverse momentum, which indicates the well-known "figure 8" motion of the electron in the relativistic laser field (45). The energy gain evolution in transverse and longitudinal directions in Fig. 7*C* illustrates that energy gain is mainly from the laser field, which is consistent with Fig. 6*E*.

An obvious feature of the electron trajectories in space, momentum, and energy is that electrons perform stochastic motion at an earlier stage and gain energy efficiently due to DLA

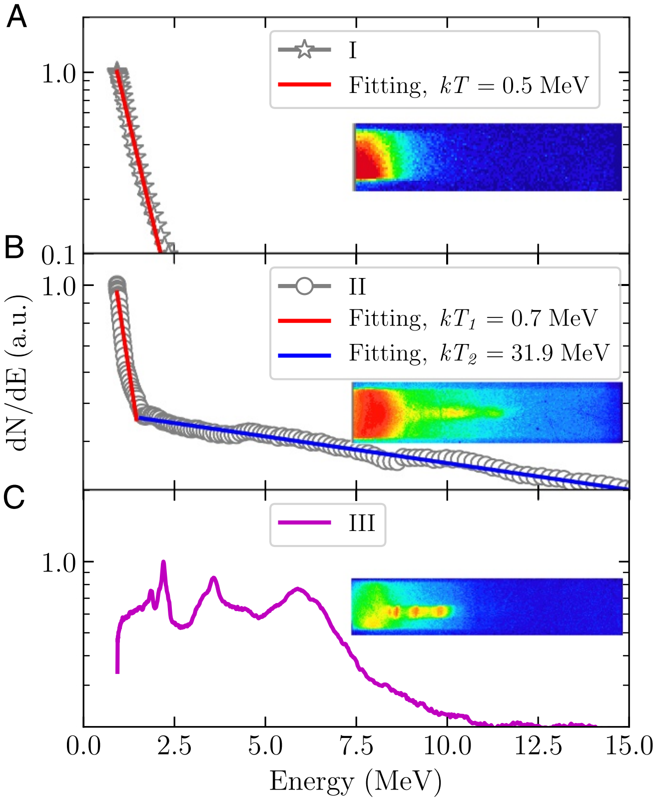

Fig. 4. (*A*–*C*) Energy spectra of the electron beams with different laser parameters: (*A*) high-contrast 2ω under the main pulse energy of 30 ± 5 J, (*B*) 1ω with high intrinsic prepulse energy under the main pulse energy of 150 J, and (*C*) 1ω with low intrinsic prepulse energy under the main pulse energy of 150 J.

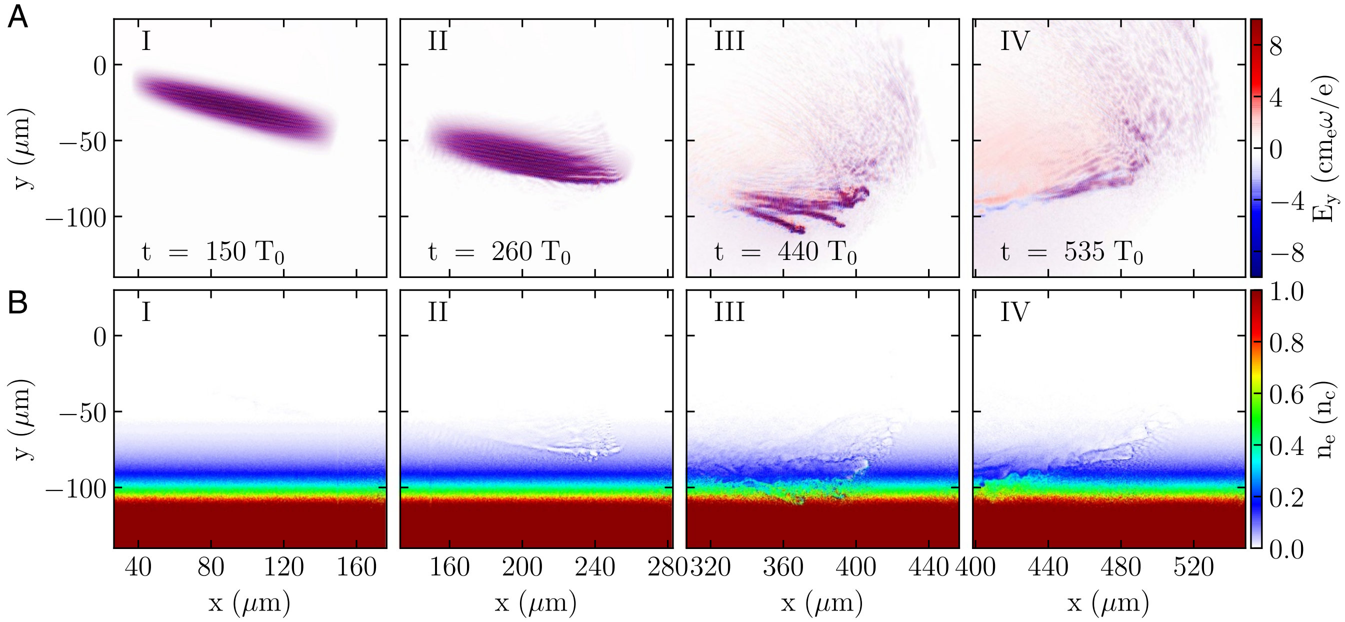

Fig. 5. Snapshots of laser fields and plasma electron density distributions at four time steps in PIC simulation. (*A*, *I–IV*) Laser field distributions. (*B*, *I–IV*) Plasma electron density distributions.

at a later stage. In Fig. 7, the vertical dashed line separates the electron trajectories into two parts. The right-hand side represents the DLA, while the left-hand side represents the stochastic heating. The stochastic motion of electrons in the laser field appears as abrupt "jumps" in electron trajectories (similar phenomena can be found in ref. 34), which act as a trigger to make the DLA happen. As deeply studied in ref. 29, efficient DLA can be triggered by stochastic motion of electrons when the laser fields exceed some threshold amplitudes, using two counterpropagating laser pulses. While in our work, the interference of the incident and reflected laser pulses results in the high-amplitude field and the enhanced stochastic motion eventually leads to the efficient DLA.

As a consequence of the collimation and acceleration inside the plasma channel, the electron spectrum agrees with that of the experiment, as shown in Fig. 6*F*. The simulated electron beam propagates along 22.1° from the x axis, close to the laser specular, with a FWHM divergence angle of 5.9°.

Our experimental observation can exclude another electron acceleration mechanism, VLA, in laser–solid interaction. In VLA, during the direct interaction with the laser field, electrons will escape the focal volume transversely after gaining

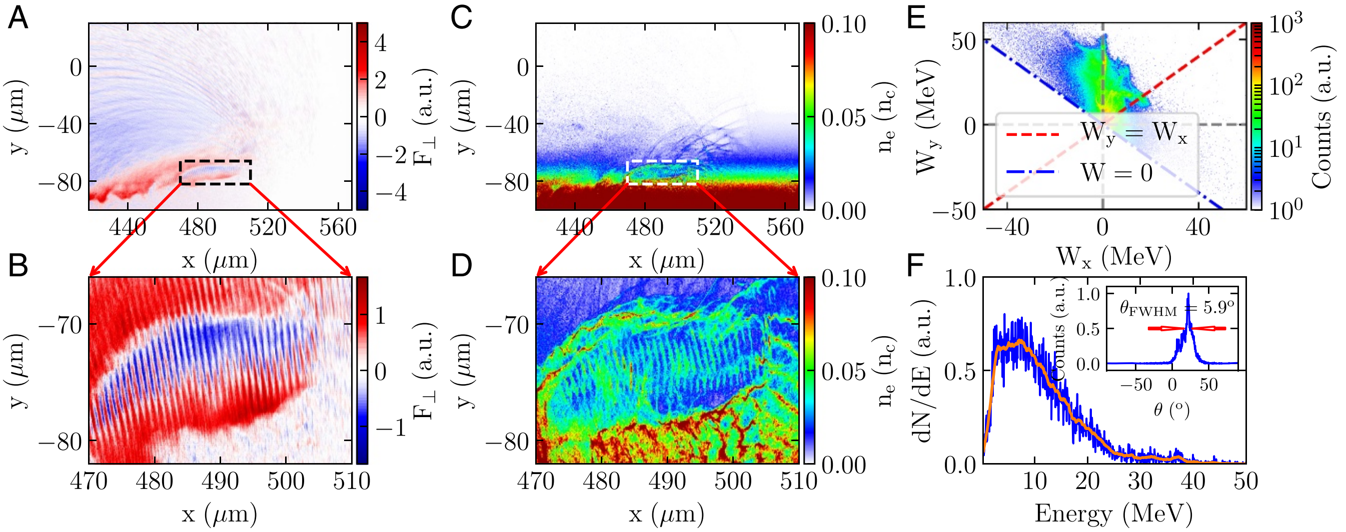

Fig. 6. (*A* and *C*) The transverse force and plasma density distribution at $t = 555\ T_0$. (*B* and *D*) The transverse focusing force and the fine structure of the electron beam distribution inside a plasma channel. (*E*) The energy gain components distribution in (W_x, W_y) space at $t = 555\ T_0$. The red dashed line divides the space into two regions: DLA-dominated region in the upper left and the wakefield acceleration-dominated region in the lower right. Electrons above the horizontal gray dashed line gain energy in the laser field while those below lose energy. Electrons to the right of the vertical dashed line gain energy from the wakefield while those to the left lose energy. (*F*) The energy spectrum of electrons escaping from the plasma at a slightly later time at $t = 585\ T_0$. *Inset* shows the corresponding angular distribution of the electron beam.

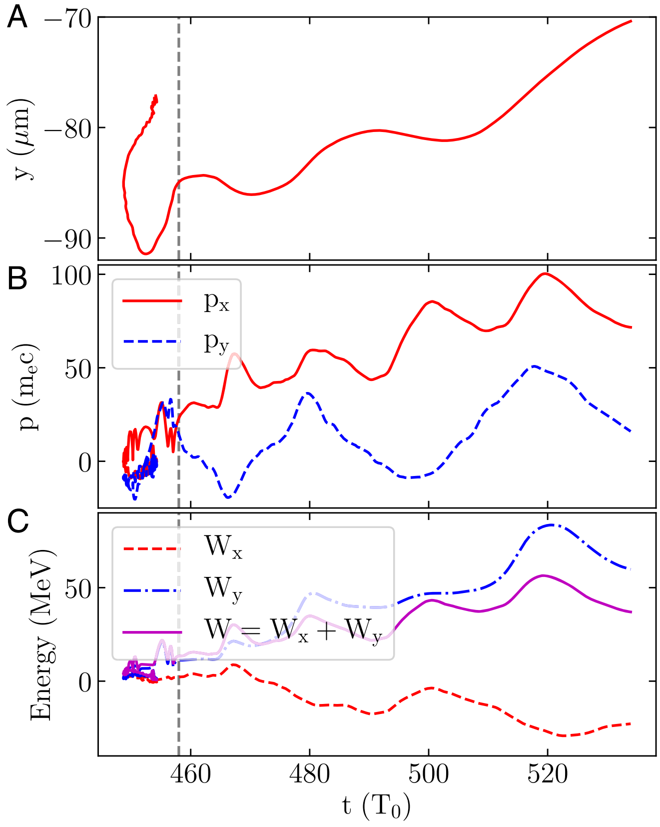

Fig. 7. Trajectories of a randomly selected electron in the plasma channel shown in Fig. 6*D*. (*A*) The spatial trajectory. (*B*) Evolution of the transverse (p_y) and longitudinal (p_x) momenta. (*C*) Evolution of the energy gain components in transverse (W_y) and longitudinal (W_x) and the total energy gain (W).

enough transverse momentum, resulting in a large beam divergence angle. Additionally, the transverse ponderomotive force tends to expel electrons from the laser axis and leads to a hollow structure in the electron beam profile, as in refs. 20, 21, and 30. However, the electron beams in our experiment are tightly collimated with small divergence angle and without the hollow structure. This reveals the importance of the self-filamentation process and the corresponding channeling process in preserving the collimation of the high-charge electron beam.

DLA in a high-density plasma channel from solid is also different from LWFA in gas, especially the so-called bubble regime in which the acceleration mainly occurs in the first wave bucket. In LWFA, the beam charge is limited to a few hundred picocoulombs due to the beam-loading effects which follow $Q \propto (k_p R_b)^4/\sqrt{n_e}$ (46), where R_b is the bubble radius. In DLA driven by a picosecond laser pulse, without the limitation of beam loading, a separate bunch of electrons can be driven in each half optical cycle. The total beam charge in simulation is proportional to the number of electron bunches in the plasma channel. The long laser pulse duration provides the energy required to sustain the continuous acceleration, and this is in accordance with the fact that the beam charge increases as the laser energy increases in experiment.

Such high-charge and high-current beams may be used to drive high-energy states of matter. Taking Au as an example, the attenuation length of the electron beam with energy of 5.3 MeV would be ∼1.5 mm, resulting in an energy density $\sim 3.3 \times 10^{12}$ J/m^3, even higher than that of the Linac Coherent Light Source (LCLS) X-ray free-electron laser (XFEL) which has been proved as a powerful tool to drive warm dense-matter states (47). The electron temperature would be on the order of ∼10 eV with mass density similar to solid density. Note that the attenuation length of megaelectronvolt electrons is much longer than that of optical laser and XFEL, which makes it an ideal tool to drive warm dense matter with a large scale. Moreover, the brightness of our electron beam, $B = 2I/\epsilon_n^2$, can be as high as 2.8×10^{16} A/m^2, provided with peak current $I = 134$ kA and normalized emittance $\epsilon_n \approx \gamma\theta\sigma = 3 \times 10^{-6}$ m, where θ is the beam divergence angle, and σ is the beam source size which is assumed the same as the laser spot size. The brightness of our electron beam is comparable to that of the highest traditional accelerators around the world (48), which makes it a promising alternative to the large-scale traditional radio frequency (RF) accelerators in various applications. Besides, the brightness of our electron beam is also orders of magnitudes higher than that of the electron beams from LWFA (7–14).

In conclusion, by using 200-TW subpicosecond laser pulses, tightly collimated (∼2.7°), directional, and nonthermal megaelectronvolt electron beams with extremely high charge (∼100 nC) were generated experimentally. The generation of such electron beams relies on the laser contrast and laser energy. Simulations illustrate an electron acceleration scenario in laser–solid interaction. In the near–critical-density plasma, the laser self-filamentation drives a bubble-like plasma channel, which confines the laser filament itself. Electrons are accelerated via DLA in each optical cycle and confined in a small region inside the plasma channel due to the ultraintense electromagnetic focusing force. In the case of long pulse duration with many optical cycles, the energy transfer from laser pulse to electron beams boosts the beam charge significantly. Such a high-charge electron accelerator might find wide applications in seeding high-flux ($\sim 2 \times 10^{11}$ photons per picosecond) γ-ray, single-shot electron radiography and even in the fast ignition concept (49). Most importantly, the extremely high-energy density of such an electron beam makes it a promising pump for warm/hot dense matter.

Materials and Methods

Laser System. Titan is a two-arm laser system with a subpicosecond west beam and a nanosecond east beam. The wavelength of both arms is 1,053 nm. The west beam was used as the main pulse, with total energy of 150 J in 700 fs pulse duration. It was focused by an f/3.5 off-axis parabola to a 7-μm 1/e^2 spot size, resulting in a laser intensity of 2.8×10^{20} W/cm^2 ($a_0 = 15$). The laser pedestal measured at 3 ns before the main pulse was 5 ± 2 mJ. By using a potassium dihydrogen phosphate (KDP) crystal for a second harmonic, the prepulse energy can be decreased to 0.2 μJ, while the energy of the main pulse is reduced to 30 ± 5 J. The east beam was used as an additional prepulse when the main pulse was at 2ω, with maximum energy at 2ω of 220 J in a 1-ns pulse duration. It was focused by an f/3.5 lens to a 38-μm 1/e^2 spot size, resulting in a laser intensity of 1×10^{16} W/cm^2. The time delay between the main pulse and the prepulse was 5 ns.

Diagnostics of the Electron Beams and the X-Ray. The angular distribution of the electron beams was measured by a pair of image plates (IP) (model Fuji-film BAS-SR 2040). They were also used to measure the beam charge (50). There were copper filters with thickness 0.3–1 mm in front of each IP to provide the ability to measure the angular distribution over different energy ranges.

Simulations were performed using the Monte Carlo N-particle transport code (MCNP) (51) to calculate the average number of X-ray photons generated by each electron, using the same parameters same as in the experiment. We found that the average number of photons generated is 0.32 per electron. The photostimulated luminescence (PSL) contribution from photons is only ∼1.6% of the electron contribution due to a much smaller sensitivity of the IP to photons than to electrons, as shown in ref. 50 for electrons and ref. 52 for photons. Therefore, the photons generated by electrons penetrating the filter can be neglected.

The energy spectra of the electron beams were measured by a spectrometer with magnetic field strength of 9,000 G and energy detection range of 0.9–49.4 MeV, which was placed behind the IPs. An X-ray pinhole camera with magnification M = 16 was used to measure the size of the plasma region.

Simulations. The simulations were performed using the PIC code EPOCH (53). The pulse duration of the incident laser is 270 fs (FWHM) with a spot size of 7 μm. The wavelength, incident angle, and polarization of the laser are the same as those in the experiment. The peak intensity of the laser is $2.8 \times 10^{20}\ \mathrm{W/cm^2}$.

The simulation box is initially located in $y \in (-140, 30)$ μm and $x \in (0, 150)$ μm with a moving window in x. The target plasma is located in $y \in (-140, -10)$ μm with density profile of $n_e = 10^{-(y+110)/25} n_c$ in y. The grid size is $\lambda_L/40$ in both directions and each cell contains 42 numerical macroparticles. The density profile is given by the radiation hydrodynamic code MULTI (54) by assuming the laser contrast is 10^{-6}.

The work done by the electric field can be split into x, y, and z:

$$W = -\frac{e}{m_e c^2} \int_0^t (E_x v_x) + (E_y v_y) + (E_z v_z) dt'. \qquad [1]$$

The EPOCH code was modified to track these components (55):

$$W_i = -\frac{e}{m_e c^2} \int_0^t E_i v_i \, dt', \ i = x, y, z. \qquad [2]$$

ACKNOWLEDGMENTS. We thank the Jupiter Laser Facility staff at LLNL for laser and technical support and Dr. Joseph Nilsen for facilitating the experiment. Yong Ma thanks W. M. Wang, L. Willingale, A. G. R. Thomas, and S. P. D. Mangles for fruitful discussions. This work was supported by the National Basic Research Program of China (Grant 2013CBA01500), the National Key R&D Program of China (Grant 2017YFA040330X), the National Natural Science Foundation of China (Grants 11334013, 11721404, and U1530150), the Chinese Academy of Sciences (CAS) key program (Grant XDB17030500), the Science Challenge Project (Grant TZ2018005), the Ministry of Science and Technology (MOST) International Collaboration (Grant 2014DFG02330), a Leverhulme Trust Research Project Grant, and the UK Engineering and Physical Sciences Research Council (EPSRC) Grant EP/N028694/1. The authors acknowledge Centre for Fusion Space and Astrophysics (CFSA) at the University of Warwick for allowing use of EPOCH.

1. Tajima T, Dawson JM (1979) Laser electron accelerator. *Phys Rev Lett* 43:267–270.
2. Rosenbluth MN, Liu CS (1972) Excitation of plasma waves by two laser beams. *Phys Rev Lett* 29:701–705.
3. Krall J, Ting A, Esarey E, Sprangle P (1993) Enhanced acceleration in a self-modulated-laser wake-field accelerator. *Phys Rev E* 48:2157–2161.
4. Sheng Z, Mima K, Sentoku Y, Nishihara K, Zhang J (2002) Generation of high-amplitude plasma waves for particle acceleration by cross-modulated laser wake fields. *Phys Plasmas* 9:3147–3153.
5. Pukhov A, Meyer-ter Vehn J (2002) Laser wake field acceleration: The highly non-linear broken-wave regime. *Appl Phys B* 74:355–361.
6. Kostyukov I, Pukhov A, Kiselev S (2004) Phenomenological theory of laser-plasma interaction in ‘bubble’ regime. *Phys Plasmas* 11:5256–5264.
7. Mangles S, et al. (2004) Monoenergetic beams of relativistic electrons from intense laser-plasma interactions. *Nature* 431:535–538.
8. Geddes C, et al. (2004) High-quality electron beams from a laser wakefield accelerator using plasma-channel guiding. *Nature* 431:538–541.
9. Faure J, et al. (2004) A laser-plasma accelerator producing monoenergetic electron beams. *Nature* 431:541–544.
10. Leemans WP, et al. (2006) GeV electron beams from a centimetre-scale accelerator. *Nat Phys* 2:696–699.
11. Hafz NAM, et al. (2008) Stable generation of GeV-class electron beams from self-guided laser-plasma channels. *Nat Photon* 2:571–577.
12. Wang X, et al. (2013) Quasi-monoenergetic laser-plasma acceleration of electrons to 2 GeV. *Nat Commun* 4:1988.
13. Kim HT, et al. (2013) Enhancement of electron energy to the multi-GeV regime by a dual-stage laser-wakefield accelerator pumped by petawatt laser pulses. *Phys Rev Lett* 111:165002.
14. Leemans WP, et al. (2014) Multi-GeV electron beams from capillary-discharge-guided subpetawatt laser pulses in the self-trapping regime. *Phys Rev Lett* 113:245002.
15. Chen LM, et al. (2001) Effects of laser polarization on jet emission of fast electrons in femtosecond-laser plasmas. *Phys Rev Lett* 87:225001.
16. Li YT, et al. (2001) Hot electrons in the interaction of femtosecond laser pulses with foil targets at a moderate laser intensity. *Phys Rev E* 64:046407.
17. Kodama R, et al. (2000) Long-scale jet formation with specularly reflected light in ultraintense laser-plasma interactions. *Phys Rev Lett* 84:674–677.
18. Li YT, et al. (2006) Observation of a fast electron beam emitted along the surface of a target irradiated by intense femtosecond laser pulses. *Phys Rev Lett* 96: 165003.
19. Habara H, et al. (2006) Surface acceleration of fast electrons with relativistic self-focusing in preformed plasma. *Phys Rev Lett* 97:095004.
20. Mordovanakis AG, et al. (2009) Quasimonoenergetic electron beams with relativistic energies and ultrashort duration from laser-solid interactions at 0.5 kHz. *Phys Rev Lett* 103:235001.
21. Tian Y, et al. (2012) Electron emission at locked phases from the laser-driven surface plasma wave. *Phys Rev Lett* 109:115002.
22. Mao JY, et al. (2012) Spectrally peaked electron beams produced via surface guiding and acceleration in femtosecond laser-solid interactions. *Phys Rev E* 85:025401.
23. Wang W, et al. (2013) Collimated quasi-monoenergetic electron beam generation from intense laser solid interaction. *High Energy Density Phys* 9:578–582.
24. Estabrook K, Kruer WL (1978) Properties of resonantly heated electron distributions. *Phys Rev Lett* 40:42–45.
25. Bulanov SV, Naumova NM, Pegoraro F (1994) Interaction of an ultrashort, relativistically strong laser pulse with an overdense plasma. *Phys Plasmas* 1:745–757.
26. Brunel F (1987) Not-so-resonant, resonant absorption. *Phys Rev Lett* 59:52–55.
27. Chen L, et al. (2001) Hot electron generation via vacuum heating process in femtosecond laser-solid interactions. *Phys Plasmas* 8:2925–2929.
28. Kruer W, Estabrook K (1985) J×B heating by very intense laser-light. *Phys Fluids* 28:430–432.
29. Sheng ZM, et al. (2002) Stochastic heating and acceleration of electrons in colliding laser fields in plasma. *Phys Rev Lett* 88:055004.
30. Thevenet M, et al. (2016) Vacuum laser acceleration of relativistic electrons using plasma mirror injectors. *Nat Phys* 12:355–360.
31. Mao JY, et al. (2015) Highly collimated monoenergetic target-surface electron acceleration in near-critical-density plasmas. *Appl Phys Lett* 106:131105.
32. Pukhov A, Sheng ZM, ter Vehn JM (1999) Particle acceleration in relativistic laser channels. *Phys Plasmas* 6:2847–2854.
33. Gahn C, et al. (1999) Multi-MeV electron beam generation by direct laser acceleration in high-density plasma channels. *Phys Rev Lett* 83:4772–4775.
34. Mangles SPD, et al. (2005) Electron acceleration in cavitated channels formed by a petawatt laser in low-density plasma. *Phys Rev Lett* 94:245001.
35. Kneip S, et al. (2008) Observation of synchrotron radiation from electrons accelerated in a petawatt-laser-generated plasma cavity. *Phys Rev Lett* 100:105006.
36. Li YY, et al. (2011) Direct laser acceleration of electron by an ultra intense and short-pulsed laser in under-dense plasma. *Phys Plasmas* 18:053104.
37. Zhang X, Khudik VN, Shvets G (2015) Synergistic laser-wakefield and direct-laser acceleration in the plasma-bubble regime. *Phys Rev Lett* 114:184801.
38. Huang TW, et al. (2016) Characteristics of betatron radiation from direct-laser-accelerated electrons. *Phys Rev E* 93:063203.
39. Willingale L, et al. (2011) High-power, kilojoule class laser channeling in millimeter-scale underdense plasma. *Phys Rev Lett* 106:105002.
40. Willingale L, et al. (2013) Surface waves and electron acceleration from high-power, kilojoule-class laser interactions with underdense plasma. *New J Phys* 15:025023.
41. Alfvén H (1939) On the motion of cosmic rays in interstellar space. *Phys Rev* 55:425–429.
42. Dodin IY, Fisch NJ (2006) Correction to the Alfvén-Lawson criterion for relativistic electron beams. *Phys Plasmas* 13:103104.
43. Sentoku Y, et al. (1999) Plasma jet formation and magnetic-field generation in the intense laser plasma under oblique incidence. *Phys Plasmas* 6:2855–2861.
44. Liu B, et al. (2013) Generating overcritical dense relativistic electron beams via self-matching resonance acceleration. *Phys Rev Lett*110:045002.
45. Kruer WL (1988) *The Physics of Laser Plasma Interactions* (Addison-Wesley, Redwood City, CA).
46. Tzoufras M, et al. (2008) Beam loading in the nonlinear regime of plasma-based acceleration. *Phys Rev Lett* 101:145002.
47. Bostedt C, et al. (2016) Linac coherent light source: The first five years. *Rev Mod Phys* 88:015007.
48. Mitri SD, Cornacchia M (2014) Electron beam brightness in Linac drivers for free-electron-lasers. *Phys Rep* 539:1–48.
49. Tabak M, et al. (1994) Ignition and high-gain with ultrapowerful lasers. *Phys Plasmas* 1:1626–1634.
50. Tanaka KA, et al. (2005) Calibration of imaging plate for high energy electron spectrometer. *Rev Scientific Instr* 76:013507.
51. Briesmeister JF (2000) MCNP: A general Monte Carlo N-Particle transport code. (Los Alamos National Laboratory, Los Alamos, NM), Technical Report LA-13709-M.
52. Maddox BR, et al. (2011) High-energy x-ray backlighter spectrum measurements using calibrated image plates. *Rev Scientific Instr* 82:023111.
53. Arber TD, et al. (2015) Contemporary particle-in-cell approach to laser-plasma modelling. *Plasma Phys Controlled Fusion* 57:1–26.
54. Ramis R, ter Vehn JM, Ramírez J (2009) {MULTI2D}–A computer code for two-dimensional radiation hydrodynamics. *Computer Phys Commun* 180:977–994.
55. Shaw JL, et al. (2017) Role of direct laser acceleration of electrons in a laser wakefield accelerator with ionization injection. *Phys Rev Lett* 118:064801.